JPhys Photonics

PURPOSE-LED PUBLISHING™

PAPER • OPEN ACCESS

Modelling thermoelastic and photoacoustic generation from polystyrene particles in microfluidic sensing platforms

To cite this article: Stefania Caragnano *et al* 2026 *J. Phys. Photonics* **8** 045016

View the article online for updates and enhancements.

This content was downloaded from IP address 193.204.188.80 on 24/11/2026 at 16:50

Journal of Physics: Photonics

Check for updates

OPEN ACCESS

RECEIVED
13 July 2026

REVISED
12 October 2026

ACCEPTED FOR PUBLICATION
4 November 2026

PUBLISHED
12 November 2026

Original content from this work may be used under the terms of the Creative Commons Attribution 4.0 licence.

Any further distribution of this work must maintain attribution to the author(s) and the title of the work, journal citation and DOI.

PAPER

Modelling thermoelastic and photoacoustic generation from polystyrene particles in microfluidic sensing platforms

Stefania Caragnano[1,2,*], Felice Alberto Sfregola[1,2], Raffaele De Palo[1], Antonio Ancona[1,2], Vincenzo Luigi Spagnolo[1], Annalisa Volpe[1,2] and Pietro Patimisco[1,*]

[1] Dipartimento Interuniversitario di Fisica, University and Polytechnic of Bari, Via Amendola 173, 70126 Bari, Italy
[2] Institute for Photonics and Nanotechnologies CNR-IFN, Via Amendola 173, 70126 Bari, Italy
[*] Authors to whom any correspondence should be addressed.

E-mail: s.caragnano@phd.uniba.it and Pietro.patimisco@uniba.it

Keywords: photoacoustics, thermoelastic deformation, finite element method (FEM), microfluidics, on-chip sensing, acoustic wave propagation, pulse duration effects

Supplementary material for this article is available online

Abstract

On-chip label-free detection of microparticles is a key challenge for developing miniaturized platforms for real-time sensing in liquids. A promising strategy involves exploiting photoacoustic and thermoelastic effects to convert optical absorption into detectable acoustic signals. Understanding these processes at the single-particle level is essential for advancing next-generation diagnostic and analytical platforms. In this work, we present a numerical investigation of the thermal, mechanical, and acoustic dynamics of a dye-free polystyrene microsphere in water under pulsed optical excitation. We developed a fully coupled finite-element model to simulate heat transfer, thermoelastic deformation, and acoustic wave propagation. The effect of optical pulse duration, from nanoseconds to milliseconds, was systematically analysed. This provides a crucial link between the temporal profile of the photonic excitation and the resulting optomechanical response. Simulations reveal a transition from an impulsive thermoelastic regime for nanosecond pulses, characterized by elastic ringing, to a quasi-static regime for longer pulses. While near-field pressure depends on pulse duration, far-field propagation becomes largely independent of excitation conditions due to acoustic attenuation in water. These findings offer key design rules for tailoring laser source specifications to optimize energy conversion efficiency. Ultimately, this work establishes a comprehensive predictive framework for the development of integrated on-chip photonics and photoacoustic sensing architectures.

1. Introduction

Microfluidic platforms enable precise control and manipulation of fluids in miniaturized channels, offering reduced sample consumption, rapid analysis and the integration of multiple analytical functions on a single chip [1–4]. Despite significant advances in device fabrication and techniques for particle manipulation in microfluidic channels, many lab-on-chip systems still rely on off-chip tools, such as microscopes or particle counters, for downstream detection [5]. This reliance limits portability and full system integration, motivating the development of on-chip sensing strategies that transform microfluidic devices from passive transport systems into fully integrated analytical platforms [6]. More recently, the possibility of exploiting photoacoustic (PA) excitation of particles directly in a microfluidic outlet well has been gaining significant attention [7, 8]. When properly designed within a microfluidic platform after the sorting stage, the outlet reservoir acts as a confined volume where particles can be optically excited, leading to thermoelastic expansion and to subsequent generation of PA waves in the surrounding liquid. The intrinsic selectivity of PA excitation stems from its spectroscopic nature: different particle materials exhibit distinct optical absorption spectra, enabling discrimination among chemically different particles that may appear morphologically identical during the sorting stage [9]. The use of broadband infrared

© 2026 The Author(s). Published by IOP Publishing Ltd

excitation sources further enhances this molecular-specific fingerprint, enabling PA-based identification suitable for particle counting and characterization. Moreover, key particle properties such as material inhomogeneities, internal discontinuities, irregular shapes, and heterogeneous structures can be discriminated by properly modelling the spectral response of the generated acoustic waves [10]. The frequency content of the emitted acoustic signal depends not only on the optical absorption properties but also on the particle size, morphology, elastic properties, and on the acoustic coupling with the surrounding fluid. As a result, particles with different internal structures or geometries produce distinct PA spectral signatures, which can be used for particle identification and classification through appropriate numerical modelling [11]. While several proof-of-concept studies demonstrated the feasibility of on-chip particle PA excitation, the thermoelastic response after PA excitation of individual microparticles is still not fully understood and has only been partially investigated in the literature [12]. This is particularly relevant for polystyrene (PS) microspheres, which are widely used as reference particles in microfluidic systems due to their well-controlled size, optical properties, and mechanical characteristics [13]. A thorough understanding of the intrinsic (i.e. dye-free) PA response of PS microparticles under pulsed laser excitation is therefore essential for the development and calibration of PA-based microfluidic sensing platforms [14]. However, this response has not yet been systematically investigated or quantified, and the relationship between thermal, elastic, and acoustic phenomena at the single-particle level remains an open research topic. For example, recent studies have demonstrated platforms that couple PA generation with surface acoustic wave (SAW) transducers to concentrate particles and convert PA signals into low-MHz SAW response for quantitative readout [15]. While these studies demonstrated the feasibility of integrating PA excitation with on-chip acousto-electric transduction, they primarily focused on ensemble measurements rather than on the physical mechanisms governing heat deposition, thermoelastic expansion, and acoustic wave generation and propagation. Furthermore, many of these studies have employed dye-stained PS microparticles, where optical absorption is dominated by the embedded dye rather than by the intrinsic polymer properties. Investigating pure PS microparticles instead would enable the study of intrinsic polymer absorption and allow operation in the infrared region, where optical scattering is reduced and PA generation is directly related to the intrinsic absorption of the material [16]. Establishing a predictive framework at the single-particle level, in dye-free conditions, is therefore essential both for interpreting experiments performed on synthetic surrogate microparticles and, most importantly, for enabling a realistic and reliable transfer of the results to biological samples under analogous excitation conditions.

In this work, we developed a first-principles, time-resolved thermoelastic model based on finite-element methods [17, 18] to characterize a single, dye-free PS microsphere suspended in water and irradiated at an intrinsic PS absorption band, where water absorption is minimal. The model couples transient heat transfer, thermoelastic deformation and acoustic wave propagation in a compressible fluid environment. By systematically varying pulse duration (from the nanosecond to the millisecond range), we identified the conditions under which impulsive or quasi-static regimes dominate and establish the baseline spectral, temporal and spatial characteristics of the emitted acoustic field. We further examined how acoustic propagation reshapes the signal spectrum, thereby bridging particle-scale physics with device-level detection metrics at prescribed standoff distances in the fluid.

2. Materials and methods

Numerical simulations were carried out in COMSOL Multiphysics 6.2 using a fully coupled, time-dependent framework to model the thermo-mechanical and acoustic response of a single PS microparticle suspended in water and irradiated by a pulsed light source.

2.1. Infrared excitation wavelength and PS absorbance

In PA excitation, accurate knowledge of the optical absorption spectrum of the target material is essential, as the generated acoustic wave is directly related to the optical absorption coefficient at the excitation wavelength. For this reason, a preliminary experimental study was conducted to identify a suitable infrared spectral region where PS exhibits significant intrinsic absorption bands while water absorption remains limited. This experimental step was necessary to ensure that PA generation originated predominantly from the PS particle rather than from the surrounding water, and to obtain a realistic value of the absorption coefficient to be used as an input parameter in the thermoelastic model. Figure 1 shows the absorption spectra of distilled water and pure PS measured by an ATR-FTIR spectrometer (Thermo scientific, iS50 ATR).

The spectra show a region around 2921 cm^{-1}, corresponding to C–H stretching vibrational mode, where PS exhibits a distinct, narrow absorption band while water absorption remains relatively low. This

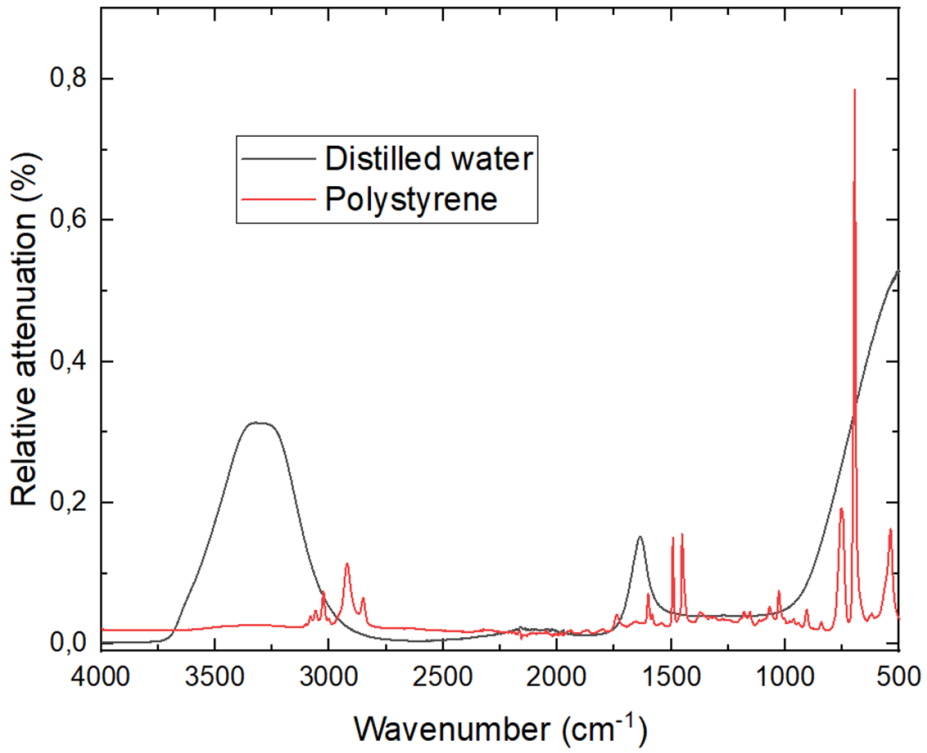

Figure 1. ATR-FTIR spectra of distilled water and pure PS, expressed as relative attenuation, $P = 100(1 - I_s/I_b)$, where I_s and I_b are the measured sample and background signals, respectively. The PS excitation wavenumber was selected near 2921 cm^{-1}.

spectral interval was therefore selected as the excitation region to maximize PA generation within the PS particle while minimizing background absorption and undesired PA generation in the surrounding water. The optical absorption coefficient of PS at 2921 cm^{-1}, $\alpha = 200$ cm^{-1}, was estimated from the logarithmic ATR absorbance, $A = -\log10(T)$, using the Beer–Lambert relation, with the ATR penetration depth taken as an approximate effective optical path length [19, 20].

2.2. Computational model

Owing to the homogeneous and isotropic properties of the material, the model was formulated using a two-dimensional axisymmetric geometry. In this framework, the 3D particle is obtained by revolving the 2D cross-section about the symmetry axis, making the solution fully representative of the three-dimensional case while significantly reducing the computational cost compared to a full 3D model. Optical scattering by the microparticle was neglected, assuming that the interaction at the selected infrared wavelength was absorption-dominated, based on an absorption coefficient of 200 cm^{-1} previously estimated for PS at 2921 cm^{-1}. This assumption was justified by the infrared excitation wavelength, for which absorption dominates over scattering and the deposited optical energy can be modelled as a volumetric heat source within the microparticle.

2.2.1. Validation of uniform volumetric absorption

To establish the reliability of the thermoacoustic model, the assumption of uniform volumetric heating within the PS particle was validated. The spatial distribution of the temperature increase was governed by the interplay between the laser pulse duration τ_{pulse} and the characteristic thermal diffusion time of the material [21, 22]. This could be quantified through the thermal diffusion length μ_{diff} which represented the distance over which heat propagated during the pulse and could be estimated, based on Fourier's law, as [21]:

$$\mu_{diff} = \sqrt{2D\tau_{pulse}} \quad (1)$$

where D was the thermal diffusivity of PS (approximately $10^{*}10^{-8}$ m^2 s^{-1} [23] (supplementary table S1)). For the shortest pulse duration discussed in this work ($\tau_{pulse} = 10$ ns), the diffusion length results $\mu_{diff} \approx 45$ nm, significantly lower than the particle radius (10 μm), indicating that the system operated under thermal confinement conditions [24]. Under these conditions, the initial temperature rise was

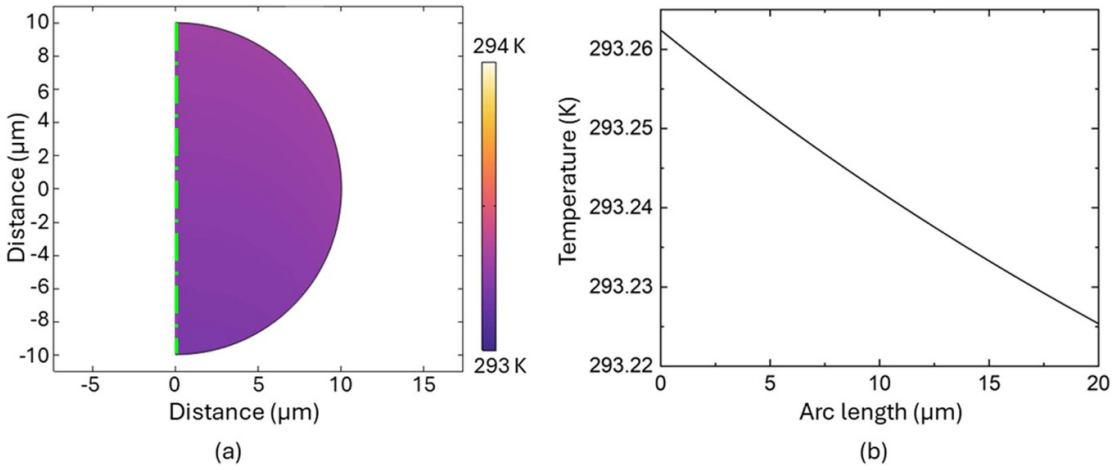

Figure 2. (a) Thermal characterization of the irradiated particle: spatial temperature distribution at the end of a 10 ns laser pulse. (b) Temperature profile as a function of arc length at $t = 10$ ns extracted along the evaluation path shown in (a) (green dotted line), which follows the axis of symmetry. The total variation remains below 0.04 K, supporting the assumption of nearly uniform heating.

governed exclusively by local optical energy absorption, with negligible heat redistribution during excitation. Moreover, the assumption remained still valid for longer pulse durations (100 ns and 1 μs), where thermal diffusion further smoothed any residual spatial gradients within the particle, reinforcing the approximation of a uniform temperature distribution. To further support this assumption, the volumetric energy absorption was explicitly simulated using COMSOL Multiphysics by coupling the *Radiative Beam in Absorbing Media* and *Heat Transfer in Solids* modules. The model considered a single PS particle with a diameter of 20 μm, irradiated by a laser pulse incident from above. Here, results for the 10 ns pulse are reported, while additional details on the simulation steps are provided in the Supplementary Information (Numerical modelling of uniform volumetric heat absorption section).

Figure 2(a) reports the temperature map of a 20 μm-diameter particle reached at the end of the laser pulse, assuming a volumetric and nearly uniform heat source. The results showed a homogeneous temperature distribution, consistent with a weakly absorbing regime.

The spatial temperature distribution along the particle axis of symmetry, indicated by the green dotted line in figure 2(a), was extracted and plotted in figure 2(b). The calculated total temperature variation was below 0.04 K, too small to constitute a significant gradient. This confirmed that heat deposition was effectively uniform throughout the particle, corresponding to an almost simultaneous temperature rise and preventing the formation of non-uniform mechanical stresses or complex phonon propagation.

2.2.2. Geometry and computational domain

The geometry of the axisymmetric computational domain is shown in figure 3. In this framework, the 2D computational domain defined in COMSOL represented a radial cross-section of a three-dimensional cylindrical structure obtained by rotation around the symmetry axis. The model consisted of a single spherical PS particle with a diameter of $d = 20$ μm suspended in a cylindrical water reservoir. The reservoir had a height h of 200 μm ($h = 10d$) and an axial length l of 2000 μm ($l = 100d$), in order to minimize boundary reflections and approximate it as an infinite fluid domain. To further reduce artificial reflections from the outer boundaries, the water domain was surrounded by a perfectly matched layer (PML) with a thickness of 100 μm, ensuring that the simulated acoustic response was not influenced by finite-domain effects within the time window of interest. This approach allowed the simulation of acoustic wave propagation in an effectively unbounded fluid domain and enabled the evaluation of the acoustic field at different standoff distances from the particle. The particle was positioned along the axis of symmetry at the centre of the water filled reservoir and was therefore assumed to be fully suspended in the fluid.

The incident radiation field was assumed to propagate along the axial direction and to impinge on the particle with a planar wavefront and a uniform intensity distribution. Light–matter interaction was modelled through volumetric optical absorption only within the PS particle, as described in the following sections. The initial temperature of both the particle and the surrounding fluid was set to 293.15 K,

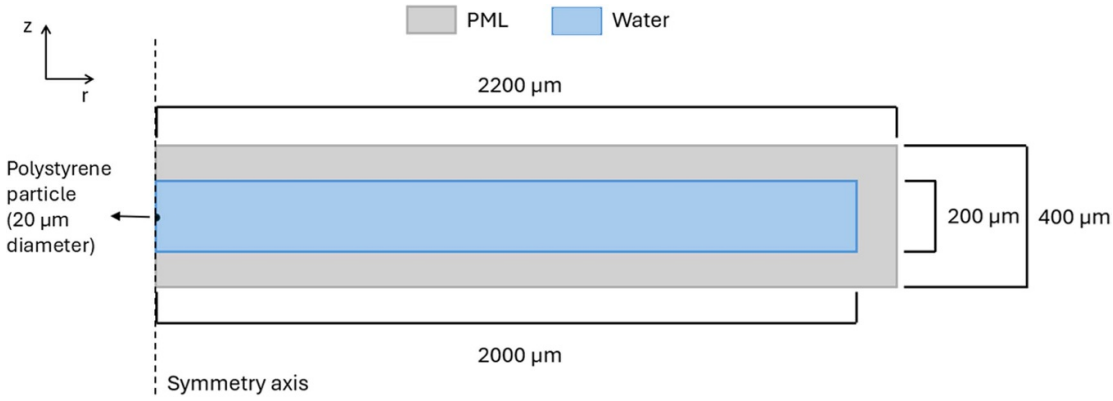

Figure 3. Schematic representation of the axisymmetric simulation domain. A single PS microparticle (20 μm diameter) was positioned along the symmetry axis at the centre of a water domain (light blue) with a height of 200 μm and an axial length of 2000 µm. The fluid domain was surrounded by a perfectly matched layer (PML, grey) with a thickness of 200 μm to prevent artificial reflections of outgoing acoustic waves at the boundaries.

and heat transfer in the liquid was assumed to occur only by conduction. Gravity, buoyancy, and convective flow in the liquid were neglected because their characteristic time scales were several orders of magnitude longer than the nanosecond duration of the laser pulse and the subsequent acoustic emission.

2.3. Material properties

Material properties for PS and water were taken from the COMSOL built-in material library and assigned to the respective domains (table S1, Supplementary). The PS particle was modelled as a linear elastic solid to account for thermoelastic deformation, while the surrounding water was modelled as a compressive acoustic medium to account for pressure wave propagation. All thermal, mechanical, and acoustic properties were assumed to be constant over the simulated temperature range.

2.4. Physics modules and multiphysics coupling

Optical absorption was preliminarily analysed in section 2.2.1. Based on these results, thermoelastic simulations were performed by replacing the optical field with an equivalent volumetric heat source.

The system response was modelled using the *Heat Transfer in Solids and Fluids* module, where optical excitation was implemented as a pulsed volumetric heat source within the PS particle. A single-pulse approximation was adopted by setting the repetition rate to 10 Hz, which was sufficiently low compared to the characteristic thermal timescales of the system. This ensured that each pulse could be treated as an independent event, avoiding cumulative heating effects, as previously reported in the literature [15].

The temporal profile of the excitation was described by a rectangular function with duration τ. This formulation accounted for laser-induced heating within the particle due to optical absorption, as well as subsequent heat diffusion into the surrounding water. Accordingly, heat transfer was solved in both the solid (PS particle) and fluid (water reservoir) domains. In the model, the optically induced heat source Q_0 was defined as [25]:

$$Q_0 = a I_0 \,\mathrm{rect}\,(\mathrm{t}) \tag{2}$$

where $I_0$is the optical intensity and $a$is the absorption coefficient of PS at 2921 cm^{-1}, as determined from the ATR analysis (section 2.1). The specific values are reported in table S2, Supplementary. The function rect(t) described the temporal modulation of the optical pulse, assuming a rectangular profile of duration τ. The mechanical response of the PS particle induced by optically generated heating was modelled using *Solid Mechanics* module, applied exclusively to the particle domain. This module was used to relate the temperature rise resulting from light absorption to the elastic deformation of the particle through thermoelastic coupling. The solid mechanics problem was governed by the momentum conservation equation [26]:

$$\nabla \cdot \sigma + \boldsymbol{F} = \rho \frac{\partial^2 \boldsymbol{u}}{\partial t^2} \tag{3}$$

where σ is the stress tensor, $\boldsymbol{F}$ represents body forces, $\rho$is the material density, and $\boldsymbol{u}$ is the displacement field. Thermoelastic coupling was included by expressing the stress tensor as a function of both mechanical strain and temperature variation, allowing the absorbed light-induced heating to generate volumetric expansion of the particle.

The propagation of the resulting pressure waves in the surrounding fluid was modelled using the *Pressure Acoustics, Transient* module, applied to the water domain. This module described the time-dependent acoustic pressure field generated by the deformation of the particle and its interaction with the fluid, yielding the acoustic response in terms of pressure signals in the surrounding medium as a function of time.

All physics modules were fully coupled within a multiphysics framework. The *Thermal Expansion* coupling was used to link the temperature field obtained from the *Heat Transfer* module to the mechanical deformation of the particle. In addition, the interaction between the deforming solid and the surrounding fluid was modelled using the *Acoustic-Structure Boundary* coupling, which transferred the normal acceleration of the particle surface to the acoustic pressure field in the fluid.

2.5. Boundary conditions and mesh

Boundary conditions were applied to all physics interfaces to ensure a physically consistent coupled thermo-mechanical and acoustic model. At the outer boundaries of the water reservoir, non-reflecting conditions were implemented using the surrounding PML (see figure 2). Continuity at the interface between the physical water domain and the PML allowed outgoing acoustic waves to be absorbed without artificial reflections, while the elongated geometry of the reservoir further minimized spurious boundary effects. At the solid–fluid interface, perfect thermal contact was assumed, ensuring continuity of temperature and heat flux. Mechanical coupling between the particle and the fluid was implemented through the acoustic–structure boundary condition.

The computational domain was discretized using free triangular meshes with element sizes tailored to each subdomain to balance accuracy and computational cost. The computational domain was discretized using free triangular elements with local refinement. The mesh was made finest inside the particle and at the solid-fluid interface, where steep thermal, mechanical, and acoustic gradients were expected, whereas in the bulk water and in the PML the element size was progressively relaxed. In the fluid domain, the maximum element size was chosen to remain smaller than a fraction of the minimum acoustic wavelength resolved in the simulations, while inside the particle it was set as a fraction of the particle diameter. To assess mesh convergence, three custom refinement levels were compared for the reference excitation case of 10 ns. Peak surface displacement, maximum temperature rise, and peak acoustic pressure were evaluated at the solid–fluid interface. Refining beyond the adopted mesh changed these quantities only by approximately 0.07%, 1.28%, and 0.12%, respectively, supporting the selected discretization. The quantitative comparison is reported in supplementary table S3.

2.6. Simulation analysis

Different response regimes of the particle were identified from the temporal evolution of temperature and deformation, providing insight into the dynamic interplay between laser heating and thermoelastic expansion. Temperature was monitored at the particle centre, while radial displacement was evaluated at the particle surface at a point along a radial direction passing through the centre. These locations were selected to track the internal thermal response and the maximum outward thermoelastic deformation along the main propagation direction. The acoustic pressure signals generated by particle deformation were monitored at multiple probe points positioned along the same radial direction. These observation points were placed at distances of 5, 20, 60, 80, 100, 150, and 200 μm from the particle surface to track the propagation and attenuation of pressure waves in the fluid. To analyse the propagation characteristics and frequency content of the acoustic waves, a fast Fourier transform (FFT) was performed on the transient pressure signals recorded at the observation points. This spectral analysis enabled the identification of dominant frequencies and the characterization of attenuation mechanisms in the fluid medium for each spectral component.

3. Results and discussion

3.1. Thermal relaxation

The thermo-mechanical response was simulated in the single-pulse regime, as the pulse separation (100 ms) was several orders of magnitude longer than the characteristic thermal relaxation time of the particle. The cooling time was first estimated using a lumped-capacitance approximation. This approach

was justified by the uniform optical energy deposition within the PS particle at the selected excitation wavelength, which resulted in an uniform initial temperature distribution inside the microsphere.

The analytical estimate was then validated against relaxation times extracted from full time-dependent simulations [21, 27]:

$$\tau = \frac{\rho c_p V}{hA} \tag{4}$$

where ρ is the particle material density, c_p is the specific heat capacity at constant pressure, V is the particle volume, and A is the surface area available for heat exchange. The heat transfer coefficient h was obtained assuming a Nusselt number close to 2, corresponding to the conduction-dominated limit for a sphere at very low-Reynolds numbers, as described by the classical Ranz–Marshall correlation [28]. This model predicted a characteristic relaxation time on the order of 100 μs for a 20 μm diameter PS sphere in water. The theoretical estimation was then compared with relaxation times extracted from the time-dependent simulations (figure 4). For each pulse duration, the characteristic cooling time was determined by fitting the exponential decay of the temperature transient following optical excitation, yielding values in the range 87–128 μs (table S4, supplementary). Since the 100 ms pulse separation exceeded the largest characteristic relaxation time by several orders of magnitude, the prediction confirmed the absence of cumulative thermal effects.

3.2. Pulse-duration-dependent thermoelastic displacement

Figure 4 shows the temporal evolution of the temperature and the resulting radial displacement of the PS particle for different laser pulse durations, spanning from the nanosecond to the millisecond regime. This range captures the transition from stress-confined thermoelastic excitation to progressively overdamped and quasi-static regimes. For clarity and representativeness, only four cases (10 ns, 100 ns, 1 μs, and 1 ms) are reported in the figure, as they exemplify the relevant regimes of the thermoelastic response, although the analysis was carried out over the entire time range. The numerical simulations revealed a strong dependence of the thermoelastic response of the PS particle on the light pulse duration. By varying the pulse duration from the nanosecond to the millisecond regime, two distinct dynamical regimes emerged, each associated with a different mechanical response and with clear implications for acoustic wave generation. In all cases, both the transient temperature and the displacement exhibited the same qualitative trend: during irradiation, the particle underwent a rapid increase in temperature and expansion, followed by relaxation back to the initial equilibrium state. However, the mechanical response changed significantly with pulse duration, revealing a clear transition from impulsive to quasistatic thermoelastic deformation. For pulse durations of 10 ns (figures 4(a) and (b)), the ultrafast energy deposition generated an impulsive thermoelastic stress on a timescale much shorter than the inertial response of the particle. This resulted in a sharp deformation peak immediately after the pulse, followed by damp elastic oscillations, characteristic of the resonant elastic ringing regime [29], in which the particle behaved as an elastic resonator that efficiently converts absorbed energy into mechanical vibration. For pulse durations in the range from 100 ns (figures 4(c) and (d)) to 1 μs (figures 4(e) and (f)), the mechanical response became progressively overdamped, with the oscillatory component largely suppressed as the excitation timescale approached the characteristic inertial timescale of the particle. Although the thermoelastic expansion still followed the rapid thermal rise, the deformation no longer exhibited pronounced ringing, marking a transition between inertial and quasistatic deformation regimes. For millisecond-long pulses (figures 4(g) and (h)), the excitation occurred on a timescale much longer than both thermal diffusion and mechanical inertia. In this quasistatic regime, the particle expanded smoothly during heating and returned monotonically to equilibrium during cooling, with no observable oscillations. In this case, the mechanical response directly followed the thermal waveform, indicating negligible inertial contributions. The transition between impulsive and quasi-static regimes was expected to have direct implications for both the efficiency of PA generation and the spectral content of the emitted acoustic waves.

3.3. PA wave generation and propagation regimes

Figure 5 shows the peak pressure values in kPa unit of the acoustic waves generated in water by the thermoelastic deformation of the PS particle, measured at a fixed near-field observation point located 5 μm from the particle surface, as a function of the laser pulse duration. The near-field analysis revealed a strong dependence of the pressure amplitude on the pulse duration, with nanosecond regime excitation producing the largest pressure transients. The rapid thermoelastic expansion associated with impulsive excitation generated sharp, high-amplitude pressure peaks, with the strongest responses occurring for pulse durations between approximately 5 and 15 ns, where the peak pressure reached around 14 kPa

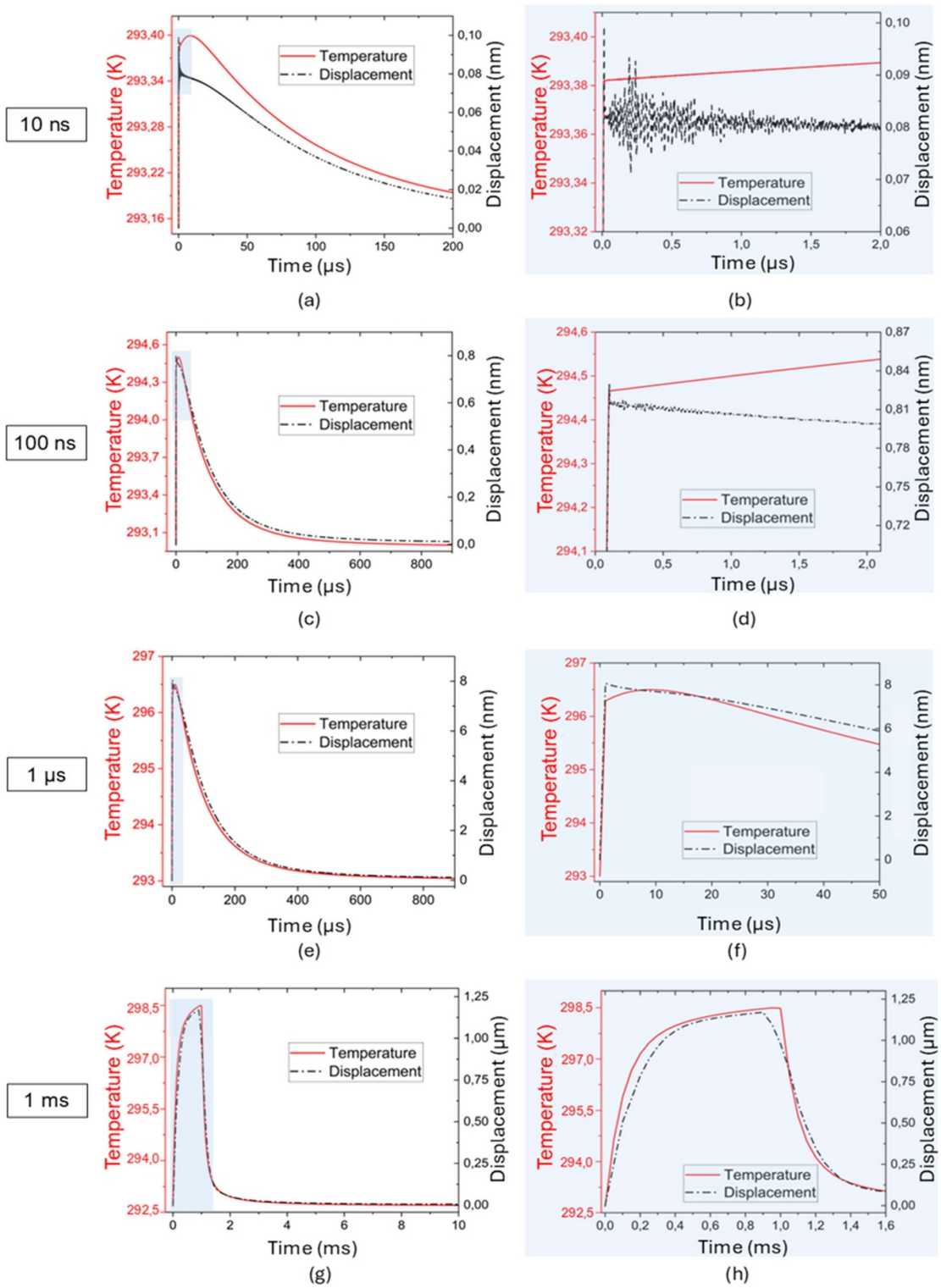

Figure 4. Temporal evolution of temperature (red solid line) and surface displacement (black dashed line) of the PS particle for optical pulses ranging from nanoseconds to milliseconds. Short pulses of 10 ns (a) and (b) produce impulsive thermoelastic stress followed by elastic ringing. Intermediate pulses of 100 ns (c) and (d) and 1 μs (e) and (f) yield small, overdamped deformation or no oscillatory behaviour, respectively. Millisecond pulses (g) and (h) lead to quasistatic thermoelastic expansion. Right panels show a magnified view of the time interval around the end of the optical pulse to highlight the onset of the mechanical response.

(figure 5(b)). As the pulse duration increased beyond ∼20–50 ns, the peak pressure began to decrease progressively. For pulse durations longer than about 100 ns, this reduction became more gradual, marking the progressive suppression of elastic ringing and the transition towards a quasi-static mechanical response. As shown in figure 5(a), extending the pulse duration into the microsecond range led to a further decay of the pressure amplitude, which approaches values lower than 1 kPa for the longest pulses.

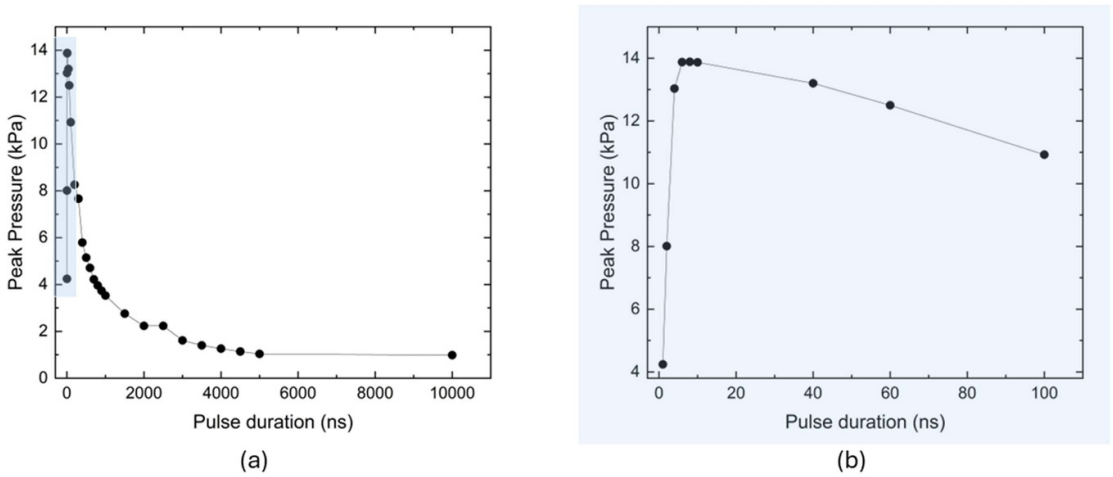

Figure 5. Pressure wave peak measured at a near-field observation point located 5 μm from the particle surface as a function of optical pulse duration. (a) Full temporals range from nanoseconds to microseconds showing the progressive decay in peak pressure with increasing pulse duration. (b) Magnified view of the nanosecond regime highlighting the sharp increase of the peak pressure obtained for pulse durations between approximately 5 and 15 ns, to the impulsive thermoelastic regime.

In this regime, the generated pressure amplitude decreased significantly, consistent with a deformation increasingly dominated by slow thermal diffusion rather than impulsive thermoelastic expansion. This behaviour marks the transition from stress-confined to quasi-static thermoelastic regimes, which directly determines the efficiency of PA generation.

Figure 6 shows the acoustic pressure waveforms generated by the thermoelastic deformation of the PS particle and recorded at increasing distances from the particle surface (5, 100, and 200 μm) for two representative pulse durations, 10 ns and 100 ns. These results illustrated the propagation of the acoustic signal in the fluid, highlighting the combined effects of amplitude attenuation and temporal delay as the wave travelled away from the source. For the 10 ns pulse (figures 6(a)–(c)), the signal in the near field was characterized by a sharp bipolar pressure transient near the particle surface, with a peak amplitude on the order of several kPa. The bipolar shape of the pressure waveform originated from the thermoelastic expansion of the particle followed by its contraction during cooling. The temporal separation between the positive and negative pressure peaks increased with pulse duration (figures 6(a)–(d)), since contraction began only after the end of the laser pulse, making the peak separation primarily governed by the temporal duration of the optical excitation. As the propagation distance increased, the waveform preserved its bipolar structure but underwent a marked reduction in amplitude together with a clear delay consistent with acoustic propagation in water. At a distance of 200 μm, the signal appeared smoother and significantly attenuated, although its impulsive nature remained recognizable. For the 100 ns pulse (figures 6(d)–(f)), the generated pressure wave was already weaker and temporally broader in the near field. During propagation, the amplitude further decreased and the waveform became more dispersed, with lower peak values and reduced high-frequency content compared to the 10 ns case. Overall, the comparison confirmed that shorter pulses generated stronger and more sharply defined acoustic transients, which remained distinguishable over longer propagation distances.

Figure 7 illustrates the evolution of the peak pressure as the acoustic wave propagated away from the particle surface for different excitation pulse durations. In the immediate vicinity of the source, the pressure amplitude strongly depended on the excitation conditions: shorter laser pulses produced significantly higher initial pressure values reaching values of approximately 14 kPa for pulse durations in the 5–15 ns range.

For an ultra-short pulse duration of 1 ns, the peak pressure is noticeably lower compared to the 10 ns case. This behaviour does not contradict stress confinement, because the reported quantity is the radiated pressure after transmission across the particle–water interface and propagation through the liquid. Shorter excitation pulses broaden the excitation bandwidth, potentially increasing the contribution of high-frequency acoustic components. These components are more strongly attenuated in water and, at sufficiently high frequencies, may be substantially suppressed over micrometric propagation distances, as will be discussed in the next session. Therefore, this frequency-dependent filtering contributes to the reduced peak pressure observed for the 1 ns pulse. The maximum in figure 5(b) should therefore be interpreted as a feature of the coupled generation, transmission, and propagation processes at the specified observation point [30, 31].

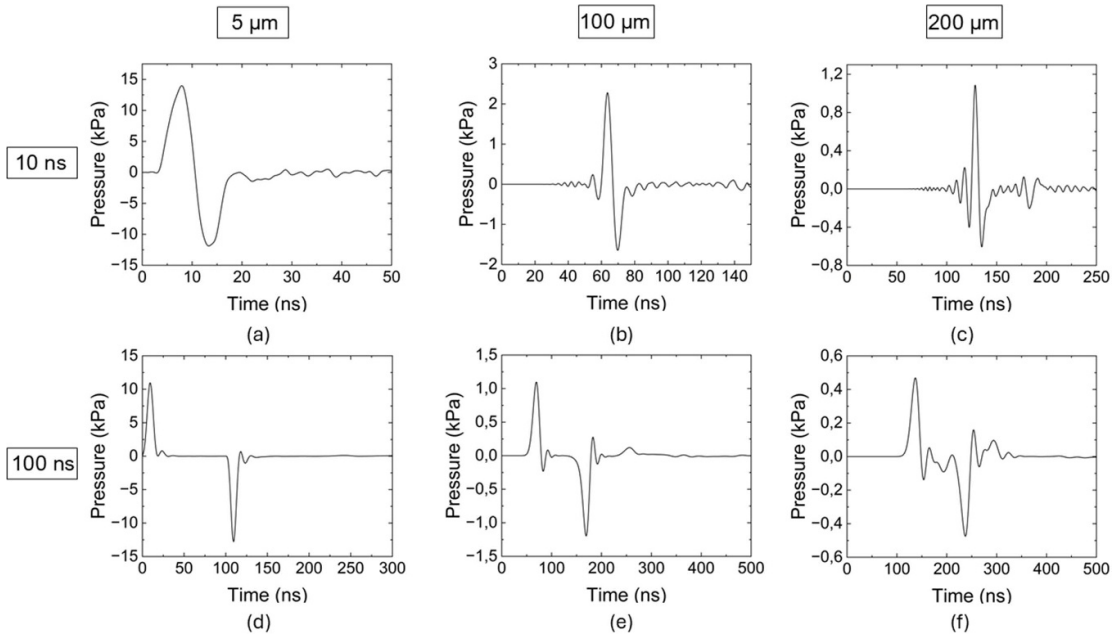

Figure 6. Acoustic pressure waveforms generated by the thermoelastic expansion of the PS particle for two pulse durations, 10 ns and 100 ns, recorded at increasing distances from the particle surface (5, 100, and 200 μm). The results show amplitude attenuation, temporal delay, and waveform broadening during propagation in water. Shorter pulses produce higher-amplitude and sharper bipolar pressure transients that remain distinguishable over longer distances.

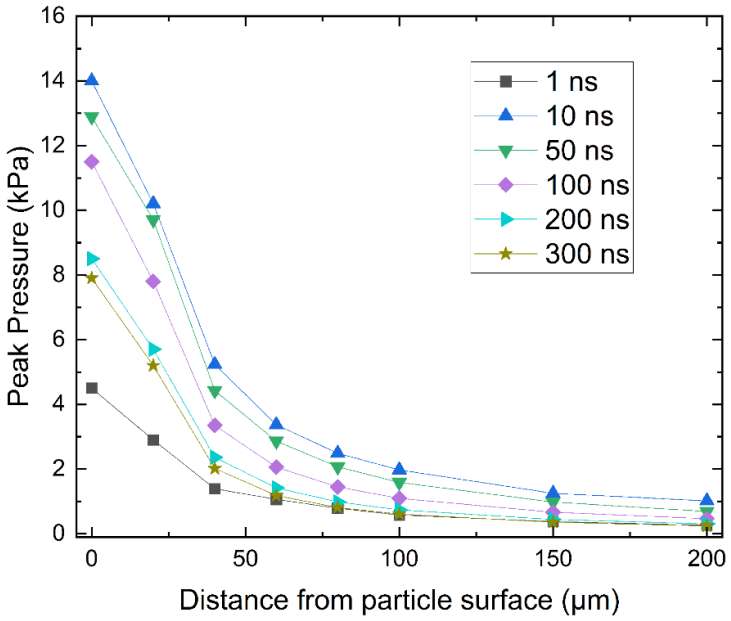

Figure 7. Peak acoustic pressure as a function of distance from the particle surface for different optical excitation pulse durations, showing the transition from a source-dominated near-field region to a propagation-dominated far-field regime.

This pronounced difference is mainly confined to the near-field region. Within the first 50 μm from the particle surface, all curves exhibited a steep attenuation, with peak pressures decreasing by approximately 70%–90% relative to their near-surface values. This rapid decay indicated that the early stage of propagation was predominantly governed by source-dependent effect, related to the thermoelastic generation mechanism. Beyond approximately 100 μm, the influence of the excitation conditions progressively diminished. The pressure amplitudes corresponding to different pulse durations converged towards similar asymptotic values, indicating that, at these distances, wave propagation was mainly governed by the intrinsic acoustic properties of water rather than by the temporal characteristics of the laser pulse. This behaviour marked the transition to a far-field acoustic regime.

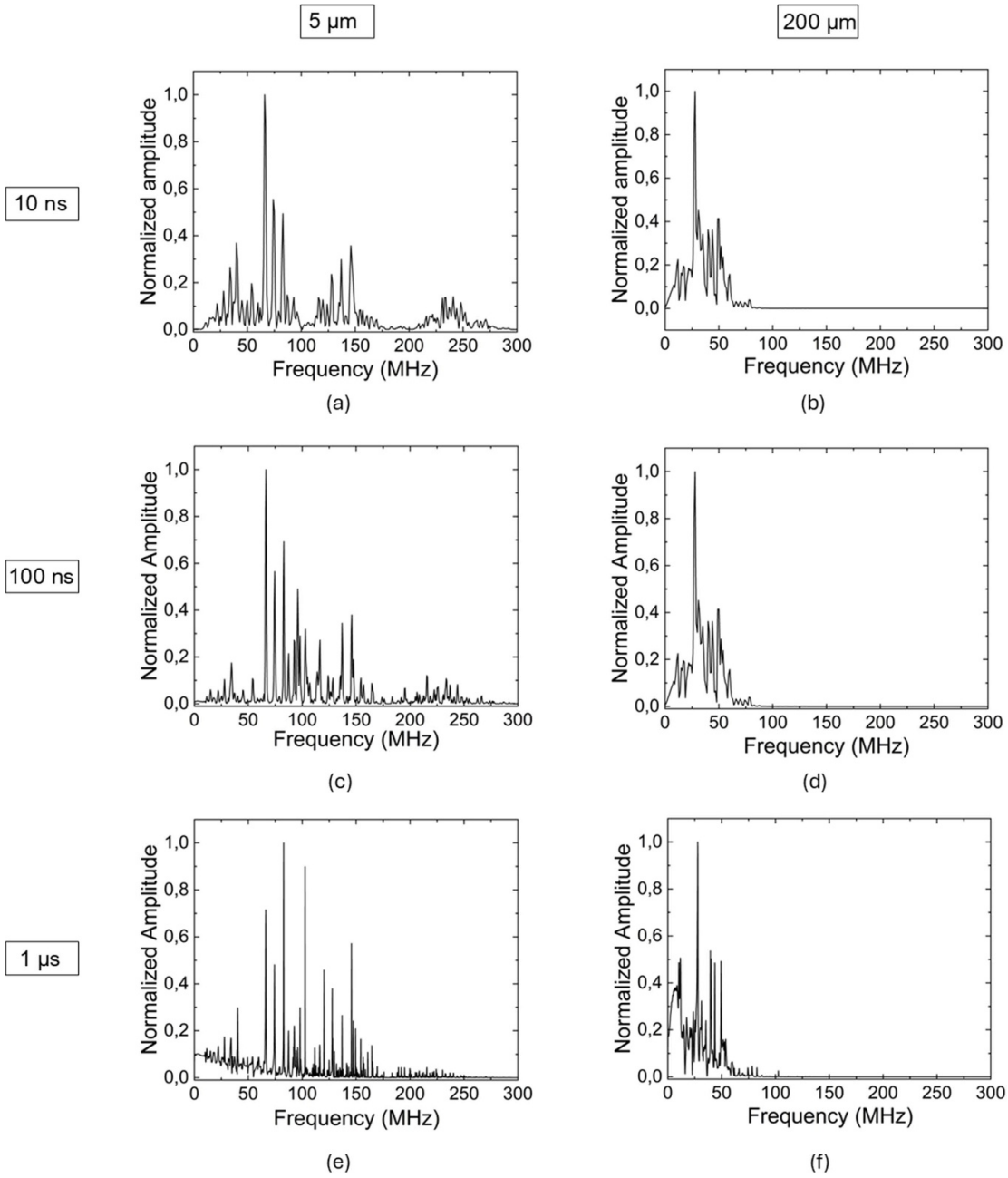

Figure 8. Normalized amplitude spectra obtained from the FFT of the simulated pressure transients for different laser pulse durations and observation distances. (a) and (b) show the spectra generated by 10 ns pulse excitation simulated at 5 μm and 200 μm distances from the particle surface, respectively. (c) and (d) report the spectra for correspond to 100 ns pulse excitation at 5 μm and 200 μm distances, respectively. (e) and (f) correspond to 1 μs pulse excitation at 5 μm and 200 μm, respectively.

Overall, these results indicate a shift from a source-dominated near-field behaviour to a propagation-dominated far-field regime, where the acoustic response becomes largely independent of the excitation pulse duration.

3.4. Frequency-domain analysis of the acoustic signal

Figure 8 shows the normalized amplitude spectra obtained from the FFT of the simulated pressure transients for three different laser pulse durations (10 ns, 100 ns, and 1 μs) and at two observation distances, 5 μm and 200 μm, representing the near-field and far-field regimes, respectively. For each excitation condition, the pressure signal was recorded at the fixed distances from the particle surface and transformed into the frequency domain (FFT) to investigate the dependence of the acoustic spectrum on pulse duration and its evolution during propagation in water.

The spectra revealed a clear distinction between short pulse and long pulse excitation regimes. For 10 ns pulses (figures 8(a) and (b)), the acoustic response was characterized by broadband spectra

extending from several tens to hundreds of MHz, with a pronounced high frequency peak associated with the elastic ringing of the particle. This behaviour was consistent with the impulsive thermoelastic regime of short pulse excitation, in which rapid stress generation produced sharp temporal features that translated into high frequency components. For intermediate pulse widths such as 100 ns (figures 8(c) and (d)), the spectra retained both low and high frequency components, indicating a hybrid regime in which quasistatic thermal expansion coexisted with reduced elastic oscillations. The presence of a broad low frequency component together with weaker high frequency peaks reflected the gradual transition between impulsive and quasistatic thermoelastic behaviour. In the long pulse regime of 1 μs (figures 8(e) and (f)), the spectral content shifted towards lower frequencies. The elastic ringing disappeared and high frequency components were suppressed, resulting in narrower spectra dominated by slow thermal expansion and relaxation processes. Figure 8 compared also spectra at two observation distances (5 μm and 200 μm). Although the overall trends with pulse duration remained consistent, the high frequency components were more strongly attenuated at 200 μm, resulting in visibly narrower spectra, indicating a strong frequency-dependent attenuation of acoustic waves in water.

These results showed that the spectral content of the acoustic signal is determined by the combined effect of the thermoelastic source dynamics and frequency-dependent attenuation during propagation, which progressively filters out high-frequency components at increasing distances.

4. Conclusions

This work presented a unified description of the thermoelastic and acoustic response of a single PS microparticle under pulsed optical excitation over a wide range of pulse duration. The simulations identified two distinct excitation regimes: an impulsive regime for nanosecond pulses and quasi-static regime for longer pulses, with an intermediate transition region around 100 ns. These regimes resulted in markedly different deformation dynamics of the particle, as well as distinct acoustic wave amplitudes and spectral characteristics in the surrounding fluid. Short pulses (5–15 ns) generated the strongest and broadband acoustic signals, with pronounced high-frequency components due to impulsive thermoelastic excitation and elastic ringing, whereas long pulses (>1 μs) produced weaker, narrowband pressure waves dominated by slow thermal expansion. Although the near-field pressure strongly depended on the excitation conditions, propagation beyond approximately 100 μm became largely independent of pulse duration, with all cases converging towards similar asymptotic pressure levels. This behaviour highlighted the dominant role of acoustic propagation in water and frequency-dependent attenuation, which progressively filtered out high-frequency components generated near the source. Overall, this study clarified the physical mechanisms governing PA emission from a single microparticle by linking thermoelastic source dynamics, spectral content, and far-field propagation. These results established a predictive framework that can support the design, optimization and interpretation of experimental PA platforms. The proposed model can be used to interpret experimental signals, optimize excitation conditions, and guide the design of detection strategies, including optical interferometric detection in water and coupling to substrate SAWs for on-chip sensing. Moreover, the present framework could be extended to multi-particle configurations to investigate collective effects and asses the limits of the current two-dimensional approximation. It could also be adapted to biological samples such as cells, vesicles, or biomolecular aggregates by adjusting material parameters and geometries. In this way, the proposed workflow bridges preliminary studies on standard PS and future investigations on biological samples, providing practical guidance for experimental design, sensitivity optimization, and efficient PA generation and detection in label-free microfluidic platforms.

Acknowledgments

This work was supported by the Ministry of University and Research (MUR) within the framework of the PNRR project PE0000023-NQSTI and the project ‘Quantum Sensing and Modeling for One-Health (QuaSiModO)’ (CUP: H97G23000100001).

Data availability statement

All data that support the findings of this study are included within the article (and any supplementary files).

Author contributions

Stefania Caragnano 0009-0001-2535-6754
Conceptualization (lead), Data curation (lead), Formal analysis (lead), Investigation (lead), Methodology (lead), Software (lead), Validation (lead), Visualization (lead), Writing – original draft (lead)

Felice Alberto Sfregola 0009-0007-7775-9970
Methodology (equal), Software (equal), Supervision (equal), Writing – review & editing (equal)

Raffaele De Palo 0000-0002-3563-2206
Conceptualization (equal), Formal analysis (equal), Methodology (equal), Supervision (equal), Writing – review & editing (equal)

Antonio Ancona
Project administration (equal), Resources (equal), Supervision (equal), Visualization (equal), Writing – review & editing (equal)

Vincenzo Luigi Spagnolo 0000-0002-4867-8166
Data curation (equal), Resources (equal), Supervision (equal), Writing – review & editing (equal)

Annalisa Volpe
Conceptualization (equal), Funding acquisition (equal), Methodology (equal), Project administration (equal), Resources (equal), Supervision (equal), Writing – review & editing (equal)

Pietro Patimisco 0000-0002-7822-2397
Conceptualization (equal), Data curation (equal), Funding acquisition (equal), Methodology (equal), Project administration (equal), Resources (equal), Supervision (equal), Validation (equal), Writing – review & editing (equal)

References

[1] Hajam M I and Khan M M 2023 Microfluidics: a concise review of the history, principles, design, applications, and future outlook *Biomater. Sci.* **12** 218–51
[2] Caragnano S, Petruzzellis I, Villarreal A I R, Terre J C, Ancona A, Osellame R, Vázquez R M and Volpe A 2025 Femtosecond laser-driven fabrication of a polymeric lab-on-a-chip for efficient size-based particle sorting in a spiral microchannel *Macromol. Mater. Eng.* **310** e00158
[3] Petruzzellis I, Martínez Vázquez R, Caragnano S, Gaudiuso C, Osellame R, Ancona A and Volpe A 2024 Lab-on-chip systems for cell sorting: main features and advantages of inertial focusing in spiral microchannels *Micromachines* **15** 1135
[4] Tan S, Qiao H, Shentu X, Xie Z, Wang Y, Liang Q, Gong X and Dai X 2025 Recent progress in microfluidic cell manipulation techniques and their applications in single-cell mass spectrometry *TrAC Trends Anal. Chem.* **196** 118630
[5] Conde J P, Madaboosi N, Soares R R, Fernandes J T, Novo P, Moulas G and Chu V 2016 Lab-on-chip systems for integrated bioanalyses *Essays Biochem.* **60** 121–31
[6] Aryal P, Hefner C, Martinez B and Henry C S 2024 Microfluidics in environmental analysis: advancements, challenges, and future prospects for rapid and efficient monitoring *Lab Chip* **24** 1175–206
[7] Liang S, Park K K, Lin W-K, Baac H W, Chen S-L and Guo L J 2025 Photoacoustic sensing and transmission for biological and industrial applications *Device* 3 100831
[8] Choi S, Kim J, Jeon H, Kim C and Park E-Y 2025 Advancements in photoacoustic detection techniques for biomedical imaging *npj Acoust.* **1** 5
[9] Durmuş H O, Birlikseven C, Karaböce B and Seyitsoy M 2022 Investigation of photoacoustic effect on different materials *2022 Medical Technologies Congress (TIPTEKNO)* (IEEE) pp 1–4
[10] Li J, Chen W and Yu B 2011 Recent progress on infrared photoacoustic spectroscopy techniques *Appl. Spectrosc. Rev.* **46** 440–71
[11] Strohm E M, Gorelikov I, Matsuura N and Kolios M C 2014 Modeling photoacoustic spectral features of micron-sized particles *Phys. Med. Biol.* **59** 5795–810
[12] Barbosa R C S and Mendes P M 2022 A comprehensive review on photoacoustic-based devices for biomedical applications *Sensors* **22** 9541
[13] Chen Q and Yuan Y J 2019 A review of polystyrene bead manipulation by dielectrophoresis *RSC Adv.* **9** 4963–81
[14] Edthofer A, Novotny J, Lenshof A, Laurell T and Baasch T 2023 Acoustofluidic properties of polystyrene microparticles *Anal. Chem.* **95** 10346–52
[15] Kishor R, Ma Z, Sreejith S, Seah Y P, Wang H, Ai Y, Wang Z, Lim T T and Zheng Y 2017 Real-time size-dependent particle segregation and quantitative detection in a surface acoustic wave-photoacoustic integrated microfluidic system *Sens. Actuators B* **252** 568–76
[16] Hang Y, Boryczka J and Wu N 2022 Visible light and near infrared fluorescence and surface enhanced Raman scattering point of care sensing and bio imaging: a review *Chem. Soc. Rev.* **51** 329–75
[17] Sfregola F A, Volpe A, Zifarelli A, Benetti M, Cannatà D, Spagnolo V and Patimisco P 2025 Full-domain 3D digital twin for comprehensive analysis and validation of standing surface acoustic wave generation on $LiNbO_3$ substrate *Adv. Mater. Technol.* **11** e01275

[18] Sfregola F A, Pizzi F, Caragnano S, De Palo R, Volpe A, Patimisco P and Jofre L 2026 Multiscale computational modeling of photoacoustic generation from micrometer-size polymeric bead suspensions in liquid media *Sci. Rep.* (https://doi.org/10.1038/s41598-026-75013-1)
[19] Larkin P J 2018 Infrared and Raman spectroscopy: principles and spectral interpretation *Appl. Spectrosc.* **72** 1278–9
[20] Kazarian S G and Chan K L A 2013 ATR-FTIR spectroscopic imaging: recent advances and applications to biological systems and pharmaceuticals *Analyst* **138** 1940–51
[21] Incropera F P, DeWitt D P, Bergman T L and Lavine A S 2007 *Fundamentals of Heat and Mass Transfer* 6th edn (Wiley)
[22] Carslaw H S and Jaeger J C 1959 *Conduction of Heat in Solids* 2nd edn (Oxford University Press)
[23] Cao Y, Chu Y, Wang Z, Qi J, Zhou L and Li Z 2021 Thermophysical properties of low-density polystyrene under extreme conditions using ReaxFF molecular dynamics *Mol. Phys.* **119** e1878304
[24] Wang L V 2009 Multiscale photoacoustic microscopy and computed tomography *Nat. Photon.* **3** 503–9
[25] Guptha K N V C S, Girish G and Manu K V 2025 Exact solutions of thermal response in pulsed laser heating under transient Dirichlet conditions with Beer–Lambert absorption model *Int. J. Adv. Eng. Sci. Appl. Math.* **17** 457–71
[26] Anand L and Govindjee S 2020 Balance laws for mass, forces, and moments *Continuum Mechanics of solids* ed S Govindjee (Oxford University Press)
[27] Yang K, Zhang X, Yang C, Zhang L and Yang H 2025 Scaling lumped transient method and thermal response evaluation of plate fin heat exchangers *Int. Commun. Heat Mass Transfer* **157** 109622
[28] Aissa A, Abdelouahab M, Noureddine A, El Ganaoui M and Pateyron B 2015 Ranz and Marshall correlations limits on heat flow between a sphere and its surrounding gas at high temperature *Therm. Sci.* **19** 1521–8
[29] Galstyan V, Pak O S and Stone H A 2015 A note on the breathing mode of an elastic sphere in Newtonian and complex fluids *Phys. Fluids* **27** 032001
[30] Diebold G J, Khan M I, Sun T and Park S M 1991 Photoacoustic monopole radiation from laser irradiated fluids *J. Acoust. Soc. Am.* **89** 1909
[31] Audoin B 2023 Principles and advances in ultrafast photoacoustics; applications to imaging cell mechanics and to probing cell nanostructure *Photoacoustics* **31** 100496